Computations of film boiling. Part I: numerical method

Asghar Esmaeeli *, Grétar Tryggvason

Mechanical Engineering Department, Worcester Polytechnic Institute, Worcester, MA 01609, USA

Abstract

A numerical method for direct simulations of boiling flows is presented. The method is similar to the front tracking/finite difference technique of Juric and Tryggvason [Int. J. Multiphase Flow 24 (1998) 387], where one set of conservation equations is used to represent the mass transfer, heat transfer, and fluid flow in the liquid and the vapor, but improves on their numerical technique by elimination of their iterative algorithm. The justification of the mathematical formulation is presented and the numerical method and the code is validated by comparison of the results with the exact solutions of a few analytical problems. A grid refinement test for film boiling on a horizontal surface shows the convergence of results.
© 2004 Elsevier Ltd. All rights reserved.

Keywords: Film boiling; Front tracking; Liquid/vapor phase change; Direct numerical simulation

1. Introduction

Boiling flows are central to many industrial and natural processes. The high heat transfer rate and the ability of fluids to store large amount of energy in the form of latent heat make boiling particularly important in large-scale energy generation and thermal energy storage. Because of the large volume change and the high temperatures involved, however, consequences of design or operational errors can be catastrophic, and accurate predictions of heat transfer and fluid flow are fundamental for safe operations. Although boiling has been studied extensively, a more basic understanding of the subject has been hindered by the small spatial and temporal scales which prevent accurate experimental measurements. Experimental and analytical studies in the past

have resulted in numerous empirical correlations, each applicable to specific conditions under which it has been developed. With the advent of numerical techniques for direct numerical simulations of boiling flows in the past few years, the prospect of using numerical simulations to study the transient and dynamic aspects of liquid/vapor phase change has become more promising. The phase change from liquid to vapor usually takes place in a highly unsteady manner where the phase boundary is very convoluted. Computations of boiling therefore require the correct incorporation of the unsteady phase boundary.

Direct numerical simulations of multifluid flows started nearly as early as computations of single-phase flows with the pioneering work of Harlow and Welch [2]. However, methods for such flows proved to be much more difficult than that for single-phase flows due to the difficulty in handling unsteady fluid interfaces. Furthermore, essentially all methods for multiphase flows have ignored phase changes. For a review of such methods see, for example, articles in a special issue of the Journal

---

* Corresponding author. Tel.: +1 508 831 5462; fax: +1 508 831 5680.

E-mail address: aesmae@wpi.edu (A. Esmaeeli).

Nomenclature

$A(t)$	amplitude	*Greek symbols*	
c	specific heat	δ	delta function
$\bar{g}$	gravity	κ	curvature
Gr	the Grashof number, $\frac{\rho_v(\rho_l-\rho_v)gl_s^3}{\mu_v^2}$	μ	viscosity
h	enthalpy	ρ	density
I	a Heaviside function	σ	surface tension
$\mathbf{I}$	Idemfactor	τ	shear stress tensor
Ja	the Jacob number, $\frac{c_v(T_w-T_{sat})}{h_{fg}}$		
k	thermal conductivity (also wave number)	*Subscripts*	
m	mass flux at the phase boundary	f	front
n	growth rate	l	liquid
$\bar{n}$	unit vector normal to the interface and pointing toward the vapor	v	vapor
		fg	(vapor–liquid)
Nu	the Nusselt number, $-\frac{ls}{(T_w-T_{sat})}\frac{\partial T}{\partial y}\big|_{y=0}$	sat	saturation
Pr	the Prandtl number, $\frac{\mu_v c_v}{k_v}$	∞	superheated
q	heat flux at the phase boundary	*Superscripts*	
T	temperature	n	time
t	time	$\cdot$	per unit time
$\bar{u}$	velocity		
$\bar{x}$	position coordinates		

of Computational Physics (volume 169), published recently.

Numerical simulations of liquid/vapor phase change have, until recently, relied on a number of simplifications. Examples of such computation can be found in Lee and Nydahl [3] who simulated the growth of a vapor nucleus at a wall, and Patil and Prusa [4] who simulated evaporation of a bubble in a superheated liquid. In both studies, however, the bubble was assumed to remain spherical during its growth. More advanced computations started with Welch [5], who simulated a fully deformable, two-dimensional bubble using moving triangular grids. He was, however, only able to follow the bubble for a relatively short time due to the distortion of the grids. Similarly, Son and Dhir [6] used a moving body-fitted coordinate system to simulate film boiling for both two-dimensional and axisymmetric flows, but were subject to similar limitations as Welch. The limitation to modest deformation of the phase boundary was overcome by Juric and Tryggvason [1] who developed a front-tracking method and Son and Dhir [7] who used a level set method. Other simulations include film boiling computations of Welch and Wilson [8] using a VOF technique, film boiling and explosive boiling computations of Esmaeeli and Tryggvason [9,10] using a front tracking/finite difference technique, film boiling computations of Shin and Juric [11] using a front tracking/level contour technique, pool-boiling computations of Dhir and collaborators [12–16] using a level set meth-

od, and nucleate boiling simulation of Yoon et al. [17] using a mesh-free method (MPS-MAFL). With the exception of [9–11], these investigations have been for two-dimensional systems.

2. Formulation and numerical method

2.1. Mathematical formulation

The governing equations for boiling flows are the conservation of mass and momentum, and the balance of thermal energy equations. In conservative forms these equations are:

$$\frac{\partial \rho}{\partial t} + \nabla \cdot \rho \bar{u} = 0, \tag{1}$$

$$\frac{\partial \rho \bar{u}}{\partial t} + \nabla \cdot \rho \bar{u}\bar{u} = -\nabla p + \rho \bar{g} + \nabla \cdot \mu(\nabla \bar{u} + \nabla \bar{u}^T), \tag{2}$$

$$\frac{\partial \rho c T}{\partial t} + \nabla \cdot \rho c \bar{u} T = \nabla \cdot k \nabla T. \tag{3}$$

Here, we neglect the viscous dissipation term in the energy equation. The above equations are valid inside each phase and at the interface the jump conditions for mass, momentum, and energy must be used:

$$\rho_l(\bar{u}_l - \bar{u}_f) \cdot \bar{n} = \rho_v(\bar{u}_v - \bar{u}_f) \cdot \bar{n} = \dot{m}, \tag{4}$$

$$\dot{m}(\bar{u}_v - \bar{u}_l) = (\boldsymbol{\tau}_v - \boldsymbol{\tau}_l) \cdot \bar{n} - (p_v - p_l)\mathbf{I} \cdot \bar{n} + \sigma\kappa\bar{n}, \tag{5}$$

$$\dot{m}h_{fg} = \dot{q} = k_v \frac{\partial T}{\partial n}\bigg|_v - k_l \frac{\partial T}{\partial n}\bigg|_l. \tag{6}$$

Here, $\bar{u}_l$ and $\bar{u}_v$ are fluid velocity at the liquid and vapor side of the interface, $\bar{u}_f$ is the interface velocity, and $\dot{m}$ is the evaporation rate at the interface. In the derivation of Eq. (6), we have assumed that the interface temperature T_f is the same as the saturation temperature at the system pressure, i.e., $T_f = T_{sat}(p_{sys})$.

In numerical implementation, we use the so-called "single-field" representation where we modify the governing differential equations such that we recover the original equations inside each phase (Eqs. (1)–(3)) and also satisfy the jump conditions at the interface (see, Appendix A). This leads to the following equations for the momentum and the thermal energy equations, respectively.

$$\frac{\partial \rho \bar{u}}{\partial t} + \nabla \cdot \rho \bar{u}\bar{u} = -\nabla p + \rho \bar{g} + \nabla \cdot \mu (\nabla \bar{u} + \nabla \bar{u}^T) + \sigma \int_F \delta(\bar{x} - \bar{x}_f)\kappa_f \bar{n}_f \, dA_f, \tag{7}$$

$$\frac{\partial \rho c T}{\partial t} + \nabla \cdot \rho c \bar{u} T = \nabla \cdot k \nabla T - \left[1 - (c_v - c_l)\frac{T_{sat}}{h_{fg}} \right] \times \int_F \delta(\bar{x} - \bar{x}_f)\dot{q}_f \, dA_f. \tag{8}$$

Here, δ is a two- or three-dimensional delta function which is constructed by repeated multiplication of one-dimensional delta functions. $\bar{x}$ is the point at which the equation is evaluated and $\bar{x}_f$ is the position of the front. The quantities with the subscript of f are evaluated at the front.

The Navier–Stokes and energy equation are supplemented by the mass conservation equation. In the past, we have solved the governing equations of multiphase fluid without phase change using a second order projection method (see, e.g., [30]). If there is no phase change, Eq. (1) is reduced to $\nabla \cdot \bar{u} = 0$ for incompressible flows and the resulting equation perfectly fits in our projection method. Here, incompressibility is satisfied within each phase but does not hold at the interface because of fluid expansion. However, it is still possible to rewrite Eq. (1) in a form that is compatible with our projection method. To do so, we note that the velocity field can be written as

$$\bar{u} = \bar{u}_v I + \bar{u}_l (1 - I), \tag{9}$$

where I is an indicator function (i.e., a Heaviside function) which is one in the vapor and zero in the liquid. Notice that this relation implies that the velocity in each phase has a smooth incompressible extension into the other phase. The gradient of the indicator function is zero everywhere except at the interface. Thus, we can express this gradient in terms of the front properties

$$\nabla I = \int_F \delta(\bar{x} - \bar{x}_f)\bar{n}_f \, dA_f. \tag{10}$$

Taking the divergence of Eq. (9), using Eq. (10), and noting that $\nabla \cdot \bar{u}_v = \nabla \cdot \bar{u}_l = 0$ yields

$$\nabla \cdot \bar{u} = \int_F \delta(\bar{x} - \bar{x}_f)(\bar{u}_v - \bar{u}_l) \cdot \bar{n}_f \, dA_f. \tag{11}$$

The difference between the velocity of the liquid and the velocity of the vapor can be related to the evaporation rate by elimination of $\bar{u}_f$ in Eq. (4) and noting that $\dot{m} = \dot{q}/h_{fg}$

$$(\bar{u}_v - \bar{u}_l) \cdot \bar{n} = \frac{\dot{q}_f}{h_{fg}}\left(\frac{1}{\rho_v} - \frac{1}{\rho_l}\right). \tag{12}$$

Inserting the expression for the velocity difference across the phase boundary from this equation into Eq. (11) yields the following mass conservation equation

$$\nabla \cdot \bar{u} = \frac{1}{h_{fg}}\left(\frac{1}{\rho_v} - \frac{1}{\rho_l}\right)\int_F \delta(\bar{x} - \bar{x}_f)\dot{q}_f \, dA_f. \tag{13}$$

Note that Juric and Tryggvason [1] formulated the mass conservation equation slightly differently.

In summary, the governing equations to solve for are Eqs. (7), (8), and (13). These equations are solved by a second order space–time accurate front tracking/finite difference method on a staggered grid. The time integration proceeds in two steps using a predictor–corrector scheme. In the next section, we first discuss a first order time integration and explain the modification to make the scheme second order afterward.

2.2. Numerical method

The phase boundary is represented by a collection of triangular elements in three-dimensions and line segments in two-dimensions. These elements are linked together by a linked-list and are used to pass information between the stationary grid and the phase boundary. At the beginning of each time step, we need to know the indicator function. This is achieved by noting that the gradient of indicator function (Eq. 10) can be computed from the front position. We take the divergence of this equation to obtain a Poisson equation for the indicator function

$$\nabla^2 I = \nabla \cdot \nabla I = \nabla \cdot \int_F \delta(\bar{x} - \bar{x}_f)\bar{n}_f \, dA_f. \tag{14}$$

The right-hand side of this equation is computed by finding $\bar{n}_f \, dA_f$ for each front element using a surface fitting (curve fitting in two-dimensions) and distributing it to the stationary grid using a smoothed delta function [29]. This equation is solved by a fast Poisson solver [31] and the fluid property fields $\phi^n \equiv (\rho^n, \mu^n, k^n, c^n)$ are found at the current time using $\phi^n = \phi_v I^n + \phi_l(1 - I^n)$, n being the time index. Next, we set the initial velocity

and the temperature fields. The heat source $\dot{q}_f$ is found using the method of Udaykumar et al. [32] by computing the right-hand side of Eq. (6) using a first order finite difference approximation.

$$\dot{q}_f = \frac{1}{\Delta}[k_v(T_v - T_{sat}) - k_l(T_{sat} - T_l)], \tag{15}$$

where T_l and T_v are the temperature of the liquid and vapor near the phase boundary at the liquid $\bar{x}_l$ and the vapor side $\bar{x}_v$. T_{sat} is the given interface temperature and T_l and T_v are found by interpolating the temperature at $\bar{x}_l = \bar{x}_f - \Delta\bar{n}_f$ and $\bar{x}_v = \bar{x}_f + \Delta\bar{n}_f$ using two normal probes which originate at the phase boundary and extend a distance Δ into the liquid and the vapor. Here, $\bar{x} = (x, y, z)$ and is measured with respect to a fixed coordinate frame. We have also experienced with a second order finite difference approximation of Eq. (6) and found no appreciable difference. Numerical experiments showed that the results are insensitive to the length of normal probes as long as $h \leqslant \Delta \leqslant 2h$, h being the grid spacing. Having found $\dot{q}_f$, the last term in Eq. (8) is then computed and distributed to the grid points using the Peskin's distribution function [29].

In the method of Juric and Tryggvason [1], the heat source was found by iteratively adjusting it until the interface temperature at the end of each time step was correct. Using the procedure described here eliminates this iteration. To move the phase boundary, we simply integrate:

$$\frac{d\bar{x}_f}{dt} = u_n\bar{n}_f, \tag{16}$$

in time, where $u_n = \bar{u}_f \cdot \bar{n}$. The normal velocity of the phase boundary can be found from Eq. (4) in conjunction with Eq. (6)

$$\bar{u}_f \cdot \bar{n} = \frac{1}{2}(\bar{u}_l + \bar{u}_v) \cdot \bar{n} - \frac{\dot{q}_f}{2h_{fg}}\left(\frac{1}{\rho_l} + \frac{1}{\rho_v}\right). \tag{17}$$

As is evident from Eq. (17), the normal velocity of the phase boundary has two components; one due to fluid advection (the first term) and another one due to phase change (the second term). The first term is found by the Peskin's interpolation [29] and the second term is found using Eq. (15). Once the right-hand side of Eq. (16) is known, a simple integration of this equation results in the position of the front at the next time step, $\bar{x}_f^{n+1} = \bar{x}_f^n + \Delta t u_n\bar{n}_f$. The indicator function at the new position I^{n+1} is then computed from Eq. (14) and the density and the heat capacity fields at the next time step, ρ^{n+1}, c^{n+1}, are found. This computation is necessary due to the use of the conservative form of the momentum and the energy equation which demands knowledge of ρ and c at the next time step $n+1$. Advection of the point is also a necessary step for implicit computation of surface tension (i.e., curvature is calculated at the next time step; κ^{n+1} rather than κ^n) which eliminates a capillary

time step constraint. At this point, we have all the information to integrate the energy equation. The energy equation in a semi-discretized form reads

$$\frac{\rho^{n+1}c^{n+1}T^{n+1} - \rho^n c^n T^n}{\Delta t} = \mathscr{A}^n, \tag{18}$$

where $\mathscr{A}$ represents the right-hand side of Eq. (8) which contains the advection, the diffusion, and the source term. The new temperature field is easily found to be

$$T^{n+1} = \frac{\Delta t \mathscr{A}^n + \rho^n c^n T^n}{\rho^{n+1}c^{n+1}}. \tag{19}$$

To solve the Navier–Stokes equation, we need to compute the surface tension term in Eq. (7) at the new position of the front, $\bar{x}_f^{n+1}$. This is done by computing the $\kappa_f\bar{n}_f \, dA_f$ for each front element using a local surface fitting in three-dimensions which involves the marked element and its three closest neighbors. In two-dimensions this is achieved by a curve fitting involving the marked element and its left and right neighbors. The surface tension is then distributed to the stationary grids using the Peskin's distribution function. The momentum equation in semi-discretized form is

$$\frac{\rho^{n+1}\bar{u}^{n+1} - \rho^n\bar{u}^n}{\Delta t} = -\nabla p + \mathscr{B}, \tag{20}$$

where the advection, the diffusion, the gravitational body force, and the surface tension force are denoted by $\mathscr{B}$. We then use a projection method and split the above equation into

$$\frac{\rho^{n+1}\tilde{\bar{u}} - \rho^n\bar{u}^n}{\Delta t} = \mathscr{B}, \tag{21}$$

and

$$\frac{\rho^{n+1}\bar{u}^{n+1} - \rho^{n+1}\tilde{\bar{u}}}{\Delta t} = -\nabla p. \tag{22}$$

Here, $\tilde{\bar{u}}$ is a provisional velocity field which is calculated in the absence of the pressure. In the first step, Eq. (21) is solved for $\tilde{\bar{u}}$ and in the second step an equation is found for the pressure by taking divergence of Eq. (22)

$$\nabla \cdot \frac{1}{\rho^{n+1}}\nabla p = \frac{\nabla \cdot \tilde{\bar{u}} - \nabla \cdot \bar{u}^{n+1}}{\Delta t} \tag{23}$$

Next, we substitute for $\nabla \cdot \bar{u}^{n+1}$ from Eq. (13) into Eq. (23). The pressure equation is solved by a multigrid solver developed by Adams [18]. Once the pressure is found, the velocity at the next time step is found from Eq. (22).

The time integration is made second order by using a predictor–corrector algorithm. Here, we are concerned with Eqs. (16), (18) and (20). If we consider ψ to represent $\bar{x}_f$, ρcT, or $\rho\bar{u}$, then these equations can be expressed as $\partial\psi/\partial t = \mathscr{F}$, where $\mathscr{F}$ represents their right-hand sides. This equation can be discretized in the predictor step as $(\psi_p^{n+1} - \psi^n)/\Delta t = \mathscr{F}^n$ and a simple integration re-

sults in $\psi_p^{n+1} = \psi^n + \Delta t \mathscr{F}^n$. The correction step should yield $\psi_c^{n+1} = \psi^n + (\Delta t/2)(\mathscr{F}^n + \mathscr{F}_p^{n+1})$. In programming, we store values of ψ^n at each time step and calculate $\psi^{n+2} = \psi_p^{n+1} + \Delta t \mathscr{F}_p^{n+1}$. We then compute $\psi_c^{n+1} = 1/2(\psi^n + \psi^{n+2})$.

In some boiling problems, there are relatively small regions of the computational domain that need a very fine grid because of presence of a steep temperature or velocity gradients, while a moderate grid is sufficient for the rest of the domain. For example, in film boiling of water at atmospheric pressure and at a low wall superheat, with the exception of the film thickness, the entire flow field can be accurately resolved with a 128 points grid per $\lambda_{d2} = 2\pi\sqrt{3\sigma/(\rho_l - \rho_v)g}$, where λ_{d2} is the most dangerous two-dimensional Taylor inviscid wavelength. On the other hand, the film thickness is about $0.004\lambda_{d2}$. Assuming that four grid points will reasonably resolve the film thickness, a uniform grid resolution of 1000 per λ_{d2} will be needed to resolve the entire domain. To simulate such flows in a computationally efficient way, one possible approach is to use a nonuniform grid where grids are clustered inside the film but a relatively coarse grid is used outside the film. We have modified our method for this purpose and introduced two sets of coordinates; the unmapped (nonuniform) one (x, y, z) and a mapped (uniform) one $(\xi(x), \eta(y), \zeta(z))$. The Navier–Stokes and energy equations are solved on the mapped grid where these equations turn out to be formally the same as those on a uniform grid but with uniform cell spacings replaced with the corresponding nonuniform ones. Here, it is still possible to solve the Poisson equation for the indicator function (Eq. 14) on the unmapped grid. However, the pressure Eq. (23) is solved on the mapped grid and its formal expression is slightly different from the corresponding one for the unmapped grid. Furthermore, the Peskin's distribution and interpolation kernels [29] are now defined with respect to the mapped (uniform) coordinate while the forces are found in the unmapped grid. The interface points are moved by interpolating their velocities on the mapped grid using Eq. (16).

3. Results

In this section we show how our numerical results compare with a few analytical solutions. We also present a grid resolution study for film boiling on a horizontal plate and discuss how our results compare with other computational results. Due to the nonlinear behavior of boiling flows, analytical solutions are only available for a few simple cases. For a comparison with other analytical solutions see Esmaeeli and Tryggvason [10], and for comparison with experimental results see part II of this study [20].

3.1. Free falling flow of a liquid/vapor layer along an inclined channel

We first study the heat transfer and fluid flow of a liquid/vapor layer falling along an inclined channel of a finite width. Here, the vapor is at the top and the liquid is at the bottom. The temperatures of the upper and the lower walls are T_v and T_l, respectively, where $T_l < T_{sat} < T_v$. This problem has a steady-state solution and was considered as the basic state by Huang and Joseph [26] in their instability analysis of a liquid/vapor interface during evaporation. Initially, the interface moves toward the lower wall as a result of the evaporation. At steady-state, the velocity and the temperature field is fully-developed and the heat fluxes at both sides of the interface are equal. As a result, phase change is stopped and the interface remains stationary thereafter. To study this problem, we used a 1×1 domain resolved by a 32×32 grid. The fluid properties were $\rho_v = 0.25$, $\rho_l = 2.5$, $\mu_v = 0.007$, $\mu_l = 0.098$, $k_v = 0.0035$, $k_l = 0.056$, $c_v = c_l = 1$, $\sigma = 0.3$ and $h_{fg} = 100$. Gravity was set to $g = 2$ and the slope of the channel was chosen to be $\theta = 30°$ ($\theta = 0°$ corresponds to a horizontal wall and $\theta = 90°$ corresponds to a vertical wall). The temperatures were set to $T_v = 4$, $T_l = -1$, and $T_{sat} = 0$. The initial position of the interface was $y = 0.8$ with respect to a coordinate attached to the lower wall. The simulation was continued until the system reached a steady-state (i.e., $y = 0.5$). Fig. 1 compares the numerical and analytical horizontal velocity profile, the pressure, the temperature, and the interface position at the steady-state. The agreement between the numerical and the analytical results are good and the relative error is less than 1% in all the cases.

3.2. Rayleigh–Taylor instability with heat and mass transfer

Our next test problems is the Rayleigh–Taylor instability of a liquid/vapor interface. Here, the interface position was at $y = 0$ and the vapor and liquid occupied the lower ($H_v \leqslant y \leqslant 0$) and the upper ($0 \leqslant y \leqslant H_l$) region of a horizontal channel, respectively. This problem has been studied analytically by Hsieh [22,23] and Hsieh and Ho [24] in the inviscid limit and by Ho [25] and Adham-Khodaparast et al. [19] in the viscous limit. The solution of the momentum and the energy equation for the basic state results in a quiescent flow and a linear temperature profile in the vapor $T_v(y) = G_v y + T_{sat}$ and the liquid $T_l(y) = G_l y + T_{sat}$. Here, $G_v = (T_v - T_{sat})/H_v$ and $G_l = (T_l - T_{sat})/H_l$ are temperature gradients in the vapor and the liquid; T_v and T_l being the temperature of the lower and the upper wall, respectively. Since the flow is quiescent, no phase change takes place at the equilibrium. As a result, the heat fluxes in the liquid and vapor are equal; $\dot{q}_{eq} = k_l G_l = k_v G_v$. For a small
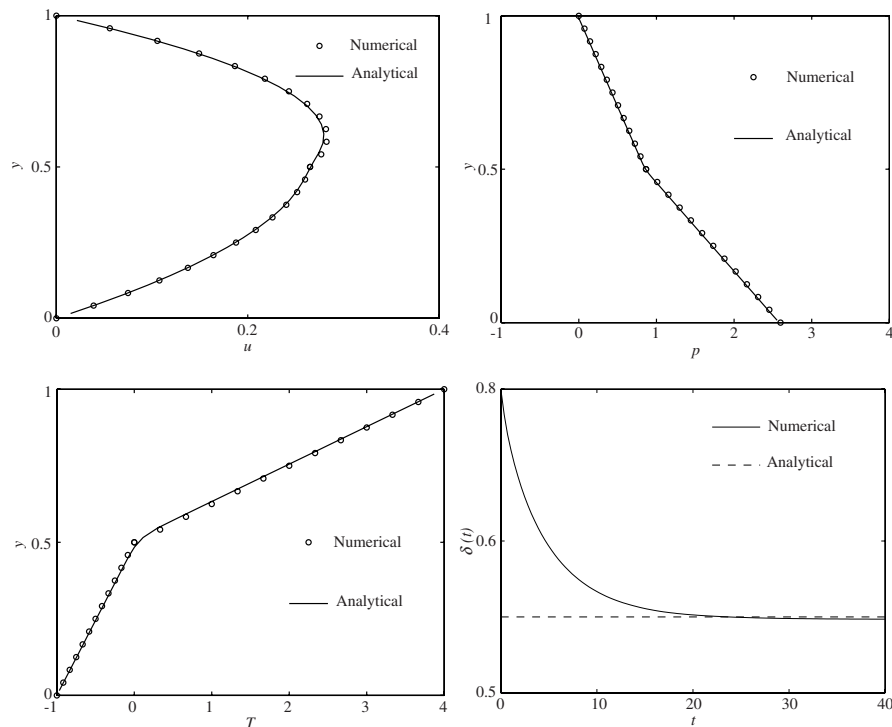
Fig. 1. Comparison of numerical and exact results for free falling flow of a two-phase mixture along an inclined channel: horizontal velocity (top-left), pressure (top-right), temperature (bottom-left), and interface position (bottom-right).

perturbation around the basic state, Hsieh [22] showed that, for inviscid flows, the evaporation at the interface reduced the growth rate of the instability. However, the critical wave number remained the same as the classical one. When viscosity is taken into consideration, Ho [25] showed that evaporation leads to a critical wave number k^*,

$$k^* = \left(\frac{4\alpha^2 v^2}{\sigma^2} + k_c^2\right)^{1/2} - \frac{2\alpha v}{\sigma},$$

which is smaller than the classical one; $k_c = \sqrt{(\rho_1 - \rho_g)g/\sigma}$. Here, $\alpha = \dot{q}_{eq}/h_{fg}(1/H_v + 1/H_1)$ is a measure of heat and mass transfer at the interface as defined by Hsieh [22].

To study this problem, we used a two-dimensional domain of size $(W_x, W_y) = (1, 2)$ and a grid resolution of 64×128. Other parameters were $\rho_1 = 2.5$, $\rho_v = 0.25$, $\sigma = 0.3$, $\mu_1 = 0.001$, $\mu_v = 0.0001$, $h_{fg} = 0.065$, $g = 12$, $T_{sat} = 0$, and $H_1 = 1$, $H_v = -1$. The initial interface position was chosen to be $y = -0.0005\cos(2\pi x)$. Thus, the wavenumber and the wavelength of the initial perturbation were $k_0 = 2\pi$ and $\lambda_0 = 1$, respectively. We carried out two sets of computations, one with phase change and another one without phase change. In the former, we set $T_v = T_1 = T_{sat} = 0$ and in the latter we set $T_v = 5$, $T_1 = -1$, and $T_{sat} = 0$. This resulted in $\alpha = 0$

for the former and $\alpha = 3.25$ for the latter. For $\alpha = 3.25$ case, the initial temperature field was also set to the temperature profile at the basic state. Fig. 2a compares the dispersion relation (i.e., growth rate versus initial wave number) for these two cases. The circles on the curves correspond to the operating conditions of this study. For this set of parameters, the cut off wave numbers for both cases are nearly the same but the growth rate for $\alpha = 0$ is $n = 5.81$ and for $\alpha = 3.25$ is $n = 4.71$ which is about 23% lower than that of the classical one, reflecting the fact that evaporation stabilizes the instability. To calculate the numerical growth rate n_N, we measured the instantaneous amplitude of the wave $A(t)$ and plotted $\ln A(t)$ versus time. If $A(t) = A_0\exp(n_N t)$, A_0 being the maximum initial amplitude, then n_N will be the slope of $\ln A(t)$ versus t curve. The measured growth rate from Fig. 2b is $n_N = 5.85$ and 4.68 for $\alpha = 0$ and $\alpha = 3.25$, respectively. This results in a 0.69% and 0.64% relative error. Similar tests in other regions of the $k - n$ space yielded relative errors in the above range.

3.3. Evaporation of a superheated liquid

The purpose of this test was to check the accuracy of our numerical scheme in simulating problems with steep temperature gradients at the phase boundary. The moti-
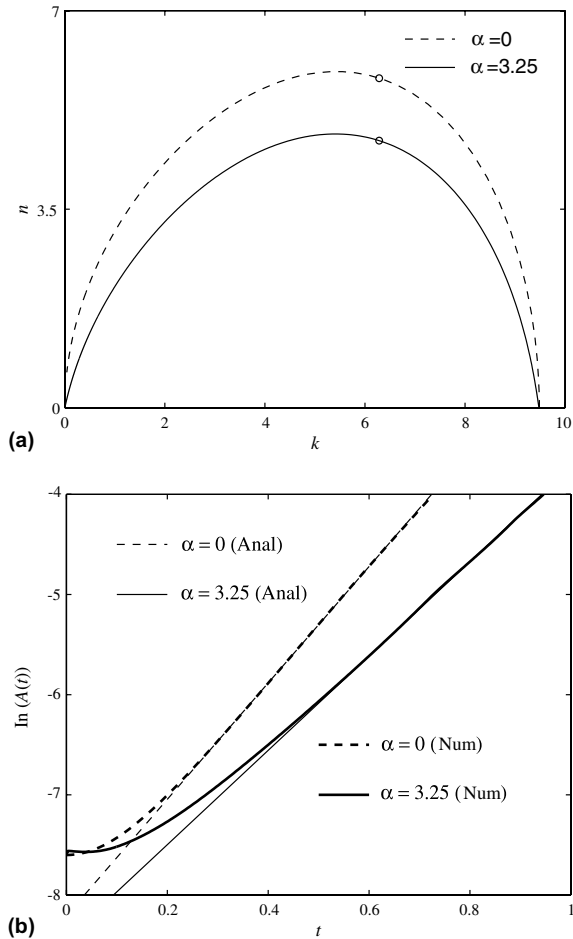
(a)

(b)

Fig. 2. (a) Dispersion relations for Rayleigh–Taylor instability with ($\alpha = 3.25$) and without ($\alpha = 0$) phase change and (b) comparison between the numerical and analytical growth rate with and without the phase change. Here, the initial wave number is 2π.

vation for this test comes from the fact that our energy solver is very sensitive to the computation of the temperature gradients at the phase boundary. In a typical phase change problem, a thermal boundary layer is usually formed at the phase boundary which results in a temperature gradient at he interface. If the thermal boundary layer grows in the course of the computations, as is the case in stable evaporation of a liquid/vapor layer, for example, the computations of the temperature gradient do not pose much difficulty. However, if the thermal boundary layer remains thin, then its accurate computations is a challenge for a numerical method. Here, we consider such a problem by investigating a test problem similar to the one used by Welch and Wilson [8].

Consider a large pool of liquid at temperature $T_\infty > T_{sat}$ resting on a solid wall. At time $t = 0$, the wall temperature is set to T_{sat} and as a result the liquid starts

to evaporate. Since the liquid is superheated, it is in a metastable state and heat is transferred at the interface from the liquid to the vapor. Conservation of mass results in $\partial v/\partial y = 0$ in both fluids. However, since the vapor layer is confined by the wall, no-through flow condition results in $v_v = 0$. $v_l(t)$ is uniform in the liquid layer and is set by the evaporation rate at the interface. Energy analysis for the vapor layer results in $T(y, t) = T_{sat}$ and the energy equation in the liquid can be cast to an ODE by using similarity transformation. This equation is solved numerically (see [8]) and its solution results in the temperature field and the interface position. We also tested the solution of the ODE by setting the densities equal, where it is possible to derive a closed form analytical solution. Thus, bulk motion is zero in both phases and solution of the energy equation in the liquid gives $T(y, t) = T_\infty + (T_{sat} - T_\infty)\,\mathrm{erfc}\,(y/2\sqrt{\alpha_l t})/\mathrm{erfc}(\gamma)$, where γ is a root of the transcendental equation $\gamma \exp(\gamma^2)\,\mathrm{erfc}\,(\gamma) = c_l(T_\infty - T_{sat})/(h_{fg}\sqrt{\pi})$. The interface position, also found as part of the solution, is $\delta(t) = 2\gamma\sqrt{\alpha_l t}$, α_l being the liquid thermal diffusivity.

To eliminate the confinement effect, we picked a 1×10 domain. Other parameters were $\delta(t_0) = 0.1$, $T_w = T_{sat} = 0$, $T_\infty = 0.5$, $h_{fg} = 1.0$, $\rho_l = 2$, $\rho_v = 0.2$, $\mu_l = 0.1$, $\mu_v = 0.01$, $k_l = 0.1$, $k_v = 0.01$, and $c_l = c_v = 0.2$. The temperature field was initialized using the temperature field from the solution of the ODE at $t = t_0$. To check the convergence rate of our results, we used grid resolutions of 16×160, 32×320, and 64×640. Although the problem is one-dimensional, the computations were carried out in two-dimensions and one-dimensional results were extracted by integrating the results in the horizontal direction. The computations were stopped before the top of the domain was affected by the thermal boundary layer. In Fig. 3a we compare the instantaneous interface locations from the computations at all the grid resolutions with the exact interface location. The exact and the computed solutions on 64×640 grid points are very close, reflecting the fact that the solution is well-converged on this grid. In Fig. 3b we make a similar comparison between the numerical and the exact liquid temperature field at a late time where it is seen that the difference between the numerical results at the finest grids and the exact solution is very small. The convergence rate was checked by computing the L_2 norm of the temperature field and the interface location and plotting these quantities on a log–log scale. As we expected, the front tracking method exhibits between linear and quadratic convergence (see, e.g., [27]).

3.4. Film boiling

We now turn to film boiling on a horizontal surface where a thin vapor layer covers a heated plate and phase change takes place at the liquid/vapor interface. The computational setup used in this study is depicted in
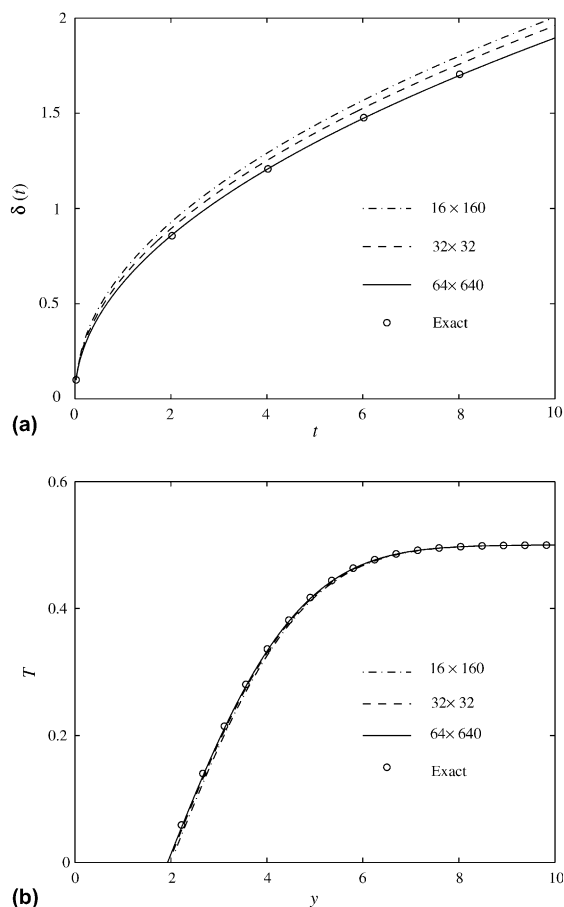
Fig. 3. Comparison of numerical and exact results for evaporation of a superheated liquid: (a) Interface position and (b) temperature profile at a late time.

the first frame of Fig. 4. An initially quiescent liquid pool rests on a hot, horizontal surface, blanketed by a thin vapor film. Initially, both the vapor and the liquid are at saturation temperature. Periodic boundary conditions are imposed at the horizontal boundaries, no-slip/no-through-flow condition at the bottom, and outflow condition at the top. The bottom wall is at a constant temperature $T_w > T_{sat}$ and the vertical temperature gradient is set to zero at the top wall. As the liquid evaporates, the liquid/vapor interface becomes unstable and bubbles are formed. At low superheats, the bubbles readily break off from the layer and rise. However, at high superheats where the vapor production is high, the bubbles are replaced by steady jets of vapor.

The governing dimensionless parameters for this problem are Gr, Pr, Ja (as defined on the nomenclature), and the ratio of thermophysical properties. Here, the individual parameters are chosen so that:

$$Pr = 4.2, \quad Gr = 17.85, \quad Ja = 0.064,$$

$$\frac{\rho_v}{\rho_l} = 0.21, \quad \frac{\mu_v}{\mu_l} = 0.386, \quad \frac{k_v}{k_l} = 0.28, \quad \frac{c_v}{c_l} = 1.83.$$

Except for the Grashof number, these parameters correspond to those of water at $p_{sat} = 169$ bar. Notice that we report the liquid properties since the method and the code have been developed for the general case where liquid could be initially subcooled.

The domain size in the horizontal directions must be equal or greater than the most dangerous three-dimensional wavelength λ_{d3}. Lao et al. [28] showed that λ_{d3} for a horizontal flat surface is given by $\sqrt{2}\lambda_{d2}$. The depth of the liquid must also be large enough to accommodate the growth of the vapor jets. Here, we use a
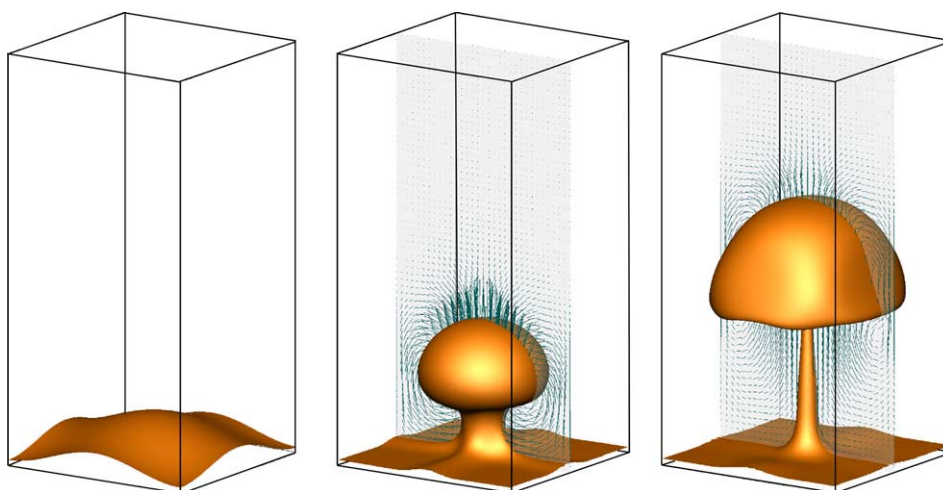

Fig. 4. Evolution of a liquid/vapor interface and velocity field during film boiling process at $Ja = 0.064$. The frames proceed from the left to the right and the times are 0, 8.38, and 16.76. Here, $Pr = 4.2$, $Gr = 17.85$, $Ja = 0.064$ and the ratio of material properties are $\rho_v/\rho_l = 0.21$, $\mu_v/\mu_l = 0.386$, $k_v/k_l = 0.28$, and $c_v/c_l = 1.83$. The domain size is $\lambda_{d3} \times \lambda_{d3} \times 2\lambda_{d3}$ and the grid resolution is $96 \times 96 \times 192$.

$\lambda_{d3} \times \lambda_{d3} \times 2\lambda_{d3}$ domain and a grid resolution of $96 \times 96 \times 192$. The initial film thickness is perturbed slightly and is given by:

$$z = z_c + \epsilon[\cos(2\pi Nx/W_x) + \cos(2\pi Ny/W_y)],$$

where, z_c, ϵ, N, W_x, and W_y are the unperturbed film thickness, perturbation amplitude, perturbation wave number, and domain size in the x and the y direction, respectively. We take $\epsilon = -0.05\lambda_{d3}$, $W_x = W_y = \lambda_{d3}$, $z_c = 0.125\lambda_{d3}$, and $N = 1$. This perturbation leads to a symmetric hump at $(x, y) = (0.5\lambda_{d3}, 0.5\lambda_{d3})$ as shown in the first frame of Fig. 4. The phase boundary is initially resolved by 46,818 triangular elements. The second and the third frames of the figure show the phase boundary and the velocity field, plotted at every third grid point, at an early and a late time. Initially, the hydrostatic pressure is maximum at the valley and minimum at the peak. This pressure difference results in a downward motion of the fluid near the valley and an upward motion near the peak and the formation of the two counter-rotating vortices on the sides of the vapor bulge. It also results in a horizontal motion of vapor from the valley toward the peak. The temperature profile in the film is approximately linear, changing from T_w at the wall to T_{sat} at the phase boundary. Therefore, the local heat flux is inversely proportional to the film thickness. As a result, as the interface moves closer to the wall, the local heat flux increases which in turn leads to further vapor production and prevents the liquid from wetting the wall. The top of the vapor dome continues to grow but evaporation prevents further thinning of the valley. The horizontal motion of the liquid near the interface widens the base of the vapor bulge and results in a mushroom-shaped bubble.

To ensure that our multimode results are well-converged, we perform a grid refinement study for a two-dimensional system. The two-dimensional system has the same nondimensional numbers as those of the three-dimensional one and is simulated in a $\lambda_{d2} \times 2\lambda_{d2}$ domain with grid resolutions of 32×64, 64×128, 128×256, and 256×512 points. The film thickness is given by

$$y = y_c + \epsilon \cos(2\pi Nx/W),$$

where $y_c = 0.125\lambda_{d2}$, $\epsilon = -0.05\lambda_{d2}$, $N = 1$, $W = \lambda_{d2}$. We also include another vapor layer on top of the liquid layer to allow rising bubbles to break through. The position of the second interface is at $1.25\lambda_{d2}$. Fig. 5a compares the phase boundaries prior to the first bubble break off ($t = 12.55$) for these grids. The convergence is very good at the base, even for the lowest grid. However, the bubble size and the vapor jet is different for the coarsest grid, but converges as the grid resolution is increased.

The Nusselt number is very sensitive to the resolution of the film. Its convergence under grid refinement is, therefore, a good indication of the convergence of the re-
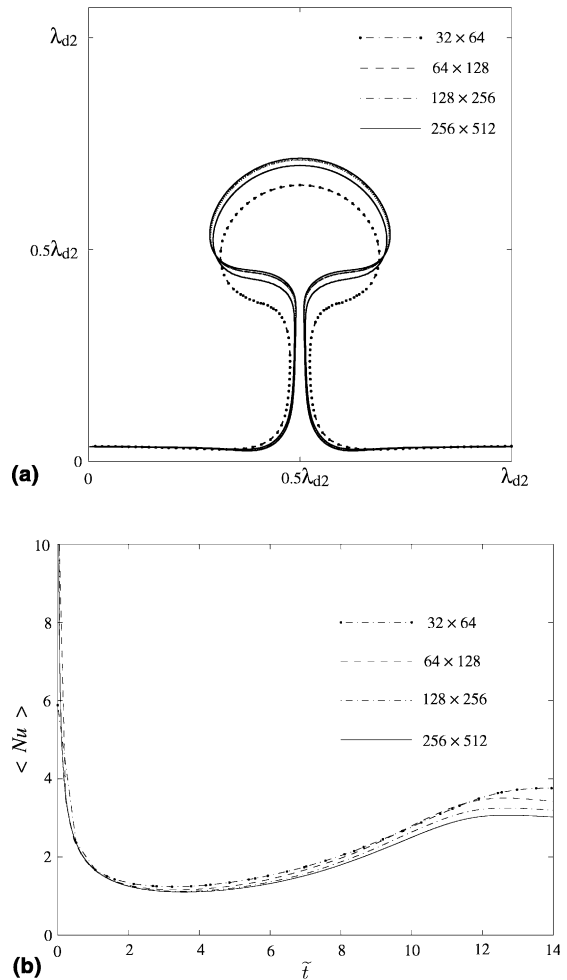

(a)

(b)

Fig. 5. Grid resolution test: (a) comparison of phase boundary before the first bubble release, and (b) $\langle Nu \rangle$ as a function of time. Here, $Pr = 4.2$, $Gr = 17.85$, and $Ja = 0.064$. The ratio of thermophysical properties are $\rho_v/\rho_l = 0.209$, $\mu_v/\mu_l = 0.386$, $k_v/k_l = 0.281$, and $c_v/c_l = 1.830$.

sults. In Fig. 5b we compare the space-averaged Nusselt number, defined as

$$\langle Nu \rangle = -\frac{l_s}{W\Delta T} \int_0^W \left.\frac{\partial T}{\partial y}\right|_w dx,$$

for these grids. The Nusselt number is initially high because of large temperature difference between the wall and the vapor in the film. When the vapor begins to warm up, the temperature gradient at the wall drops down and $\langle Nu \rangle$ decreases. The Nusselt number, however, starts to increase again as a bubble is formed and the average film thickness starts to decrease. The figure shows convergence of $\langle Nu \rangle$ under the grid refinement. We have continued the run on the 64×128 grid and the one on the 128×256 grid up to $\tilde{t} = 279$ (i.e., over seven bubble release period) and calculated the

time-averaged Nusselt number defined as $\overline{\langle Nu \rangle} = 1/\Delta t \int_{t_i}^{t_e} \langle Nu \rangle \, dt$, where $\Delta t = t_e - t_i$, and t_i and t_e are the beginning time of the steady-state and the end-time of the simulation, respectively. The results are 2.19 for the 64×128 grid and 2.08 for the 128×256 grid, or about 5% relative error. Fig. 5b suggests that the difference between the 128×256 grid and even finer grids would be much smaller.

3.5. Other tests

We have also tested our code by comparing our results with the film boiling simulation in Fig. 12 of Welch and Wilson [8] and Fig. 2 of Juric and Tryggvason [1]. These simulations correspond to evaporation of Hydrogen and para-Hydrogen at 8 atm. We used the same initial conditions and comparable grid resolutions. In both cases the interface evolved into a similar mushroom shape. We measured the dimensions of the mushroom (i.e., height, length of the arms, etc.) and found a good agreement between our results and theirs.

The method described here has been used to study multimode film boiling on horizontal surfaces [20], explosive boiling [10], and boiling in complex geometries [21]. In all of these problems, the qualitative behavior of the interface, temperature field, and the velocity field were similar to those observed in experiments. The agreement between the numerical results and experimental results were also good, in those cases when it was possible to make such comparisons [10,20].

4. Conclusion

A front tracking/finite difference technique for computations of boiling flows is presented. The method is based on the so-called "single-field formulation" where one set of the conservation equations is written for both phases. The method and the code was validated by comparing the numerical results with a few analytical solutions and a grid refinement study of film boiling on a horizontal plate.

Acknowledgment

Appendix A. Detail of derivation of the single-field equations

The governing Eqs. (1)–(3) can be written in the following canonical form

Table 1
Canonical form of the conservation equations

Equation	ϕ	ψ	S
Mass	ρ	$\rho \bar{u}$	0
Momentum	$\rho \bar{u}$	$\rho \bar{u} \bar{u} - \tau + p\mathbf{I}$	$\rho \bar{g}$
Energy	$\rho c T$	$\rho c \bar{u} T - k \nabla T$	0

$$\frac{\partial \phi}{\partial t} + \nabla \cdot \boldsymbol{\psi} = S, \tag{A.1}$$

where ϕ is the conserved quantity, $\boldsymbol{\psi}$ is a combination of its flux and some other fluxes, and S is a source term as shown in (Table 1). Integration of (A.1) over a vanishingly small volume which encloses the phase boundary and is moving with the phase boundary leads to

$$[[\phi]]_v^l u_n = [[\boldsymbol{\psi}]]_v^l \cdot \bar{n}, \tag{A.2}$$

as the corresponding jump condition of the conservation equation (see [33], for example). Here, $u_n = \bar{u}_f \cdot \bar{n}$. These are the so-called Rankine–Hugoniot or shock conditions and may be considered as "pseudo" jump conditions since they do not take into account interfacial quantities such as surface tension and latent heat. Thus, the "true" jump conditions are Eqs. (4)–(6) which are derived directly by writing the balance laws at the interface.

Application of Eq. (A.2) to Eqs. (1)–(3), and some algebraic manipulations, result in the following pseudo jump conditions:

$$\rho_l(\bar{u}_l - \bar{u}_f) \cdot \bar{n} = \rho_v(\bar{u}_v - \bar{u}_f) \cdot \bar{n} = \dot{m}, \tag{A.3}$$

$$\dot{m}(\bar{u}_v - \bar{u}_l) = (\tau_v - \tau_l) \cdot \bar{n} - (p_v - p_l)\mathbf{I} \cdot \bar{n}, \tag{A.4}$$

$$\dot{m}(c_v - c_l)T_{sat} = k_v \frac{\partial T}{\partial n}\Big|_v - k_l \frac{\partial T}{\partial n}\Big|_l. \tag{A.5}$$

Comparison of Eqs. (A.3) and (4) shows that the true and pseudo jump conditions are the same for conservation of mass, as expected. On the other hand, comparison of the true and pseudo jump conditions for the momentum and energy shows that $\sigma \kappa \bar{n}$ and $\dot{m}((c_v - c_l)T_{sat} - h_{fg})$ are missing in the pseudo jump equations of momentum and energy, respectively. These terms are supplemented to Eqs. (2) and (3) by using a delta function which is nonzero at the phase boundary and diminishes away from the interface. Notice that we have used $\dot{m} = \dot{q}/h_{fg}$ in the energy equation and also taken advantage of the fact that the thermophysical properties such as c_l, c_v, and σ are constant.

References

[1] D. Juric, G. Tryggvason, Computations of boiling flows, International Journal of multiphase flow 24 (1998) 387–410.

[2] F.H. Harlow, J.E. Welch, Numerical calculation of time-dependent viscous incompressible flow of fluid with a free surface, Physics of Fluids 8 (1965) 2182–2189.

[3] R.C. Lee, J.E. Nydahl, Numerical calculations of bubble growth in nucleate boiling from inception through departure, ASME Journal of Heat Transfer 111 (1989) 474–479.

[4] R.K. Patil, J. Prusa, Numerical solutions for asymptotic, diffusion controlled growth of a hemispherical bubble on an isothermally heated surface, in: M.F. Modest, T.W. Simon, A. Ebadian (Eds.), Experimental/Numerical Heat Transfer in Combustion and Phase Change, HTD-vol. 170, ASME, New York, 1991.

[5] S.W.J. Welch, Local simulation of two-phase flows including interface tracking with mass transfer, Journal of Computational Physics 121 (1995) 142–154.

[6] G. Son, V.K. Dhir, Numerical simulation of saturated film boiling on a horizontal surface, ASME Journal of Heat Transfer 119 (1997) 525–533.

[7] G. Son, V.K. Dhir, Numerical simulation of film boiling near critical pressures with a level set method, ASME Journal of Heat Transfer 120 (1998) 183–192.

[8] S.W.J. Welch, J.J. Wilson, A volume of fluid based method for fluid flows with phase change, Journal of Computational Physics 160 (2000) 662–682.

[9] A. Esmaeeli, G. Tryggvason, Direct numerical simulations of boiling flows, in: Proceedings of the Fourth International Conference on Multiphase Flow, ICMF-2001, New Orleans, Louisiana.

[10] A. Esmaeeli, G. Tryggvason, Computations of explosive boiling in microgravity, Journal of Scientific Computing 19 (2003) 163–182.

[11] S. Shin, D. Juric, Modeling three-dimensional multiphase flow using a level contour reconstruction method for front tracking without connectivity, Journal of Computational Physics 180 (2002) 427–470.

[12] D. Banerjee, V.K. Dhir, Study of subcooled film boiling on a horizontal disc: Part I—Analysis, ASME Journal of Heat Transfer 123 (2001) 271–284.

[13] D. Banerjee, V.K. Dhir, Study of subcooled film boiling on a horizontal disc: Part II—Experiments, ASME Journal of Heat Transfer 123 (2001) 285–293.

[14] V.K. Dhir, Numerical simulations of pool-boiling heat transfer, AIChE Journal 47 (2001) 813–834.

[15] G. Son, V.K. Dhir, N. Ramanujapu, Dynamics and heat transfer associated with a single bubble during nucleate boiling on a horizontal surface, ASME Journal of Heat Transfer 121 (1999) 623–631.

[16] G. Son, N. Ramanujapu, V.K. Dhir, numerical simulation of bubble merger process on a single nucleation site during pool nucleate boiling, ASME Journal of Heat Transfer 124 (2002) 51–62.

[17] H.Y. Yoon, S. Koshizuka, Y. Oka, Direct calculation of bubble growth, departure, and rise in nucleate pool boiling, International Journal of Multiphase Flow 27 (2001) 277–298.

[18] J. Adams, MUDPACK: multigrid FORTRAN software for the efficient solution of linear elliptic partial differential equations, Applied Mathematics and Computation 34 (1989) 113–146.

[19] K. Adham-Khodaparast, M. Kawaji, B.N. Antar, The Rayleigh–Taylor and Kelvin–Helmholtz stability of a viscous liquid–vapor interface with heat and mass transfer, Physics of Fluids 7 (1995) 359–364.

[20] A. Esmaeeli, G. Tryggvason, Computations of film boiling, Part II—Multimode film boiling, International Journal of Heat Mass Transfer, in press.

[21] A. Esmaeeli, G. Tryggvason, A front tracking method for computations of boiling in complex geometries, International Journal of Multiphase Flow 30 (2004) 1037–1050.

[22] D.Y. Hsieh, Interfacial stability with mass and heat transfer, Physics of Fluids 21 (1978) 745–748.

[23] D.Y. Hsieh, Effects of heat and mass transfer on Rayleigh–Taylor instability, Journal of Basic Engineering 94 (1972) 156–162.

[24] D.Y. Hsieh, S.P. Ho, Rayleigh–Taylor stability with mass and heat transfer, Physics of Fluids 24 (1981) 202–208.

[25] S.P. Ho, Linear Rayleigh–Taylor stability of viscous fluid with mass and heat transfer, Journal of Fluid Mechanics 101 (1980) 111–128.

[26] A. Huang, D.D. Joseph, Stability of liquid–vapor flow down an inclined channel with phase change, International Journal of Heat Mass Transfer 36 (1993) 663–672.

[27] R.J. LeVeque, Z. Li, The immersed interface method for elliptic equations with discontinuous coefficients and singular sources, SIAM Journal of Numerical Analysis 31 (1994) 1019–1044.

[28] Y.-J. Lao, R.E. Barry, R.E. Balzhiser, A study of film boiling on a horizontal plate, Paper B3.10, Fourth International Heat Transfer Conference, Paris, Versailles, "heat transfer 1970" vol. V, Elsevier, Amsterdam, 1970.

[29] C.S. Peskin, Numerical analysis of blood flow in the heart, Journal of Computational Physics 25 (1977) 220–252.

[30] G. Tryggvason, B. Bunner, A. Esmaeeli, D. Juric, N. Al-Rawahi, W. Tauber, J. Hans, S. Nas, Y.-J. Jan, A front-tracking method for the computing of multiphase flow, Journal of Computational Physics 169 (2001) 708–759.

[31] U. Schumann, R. Sweet, A direct method for the solution of Poisson's equation with boundary conditions on a staggered grid of arbitrary size, Journal of Computational Physics 20 (1976) 171–182.

[32] H.S. Udaykumar, W. Shyy, M.M. Rao, ELAFINT: a mixed Eulerian–Lagrangian method for fluid flows with complex and moving boundaries, International Journal for Numerical Methods in Fluids 22 (1996) 691–712.

[33] C. Hirsch, Numerical computations of internal and external flowsFundamentals of Numerical Discretization, vol. 1, Wiley, New York, 1988, pp. 88–90.